# Time-dependent analysis of the breakup of halo nuclei

P. Capel and D. Baye
*Physique Quantique, C.P. 165/82 and Physique Nucléaire Théorique et Physique Mathématique, C.P. 229, Université Libre de Bruxelles, B-1050 Brussels, Belgium*

V. S. Melezhik
*Department of Physics and Astronomy, California State University at Long Beach, Long Beach, California 90840, USA and Joint Institute for Nuclear Research, Dubna, Moscow Region 141980, Russian Federation*
(Received 8 April 2003; published 29 July 2003)

The breakup of halo nuclei is studied by numerically solving the semiclassical time-dependent Schrödinger equation on an angular Lagrange mesh and on a quasiuniform radial mesh. The merits of different mesh choices and approximations of the time evolution operator are discussed. The numerical technique is applied to the breakup of the $^{11}$Be and $^{15}$C halo nuclei at energies around 70 MeV/nucleon. The time evolution of the projectile wave packet during the breakup process is visualized. The role of the nuclear interaction between target and projectile is analyzed and the validity of pure Coulomb breakup with an impact parameter cutoff is estimated. The breakup and inelastic cross sections are discussed and compared with available experimental data.

DOI: 10.1103/PhysRevC.68.014612 PACS number(s): 25.60.Gc, 25.70.De, 02.70.Jn, 27.20.+n

## I. INTRODUCTION

Halo nuclei are among the most fascinating quantal systems [1]. The mean radii of the orbitals of some among their nucleons can be larger than the range of the nuclear interaction with other nucleons. This topic is the subject of intensive experimental investigations. Breakup is one of the most useful tools for studying the properties of halo nuclei. In these reactions, information coming from the dissociation of the projectile into fragments can be used to infer the properties of the halo part of the wave function. Coulomb breakup is of particular interest because uncertainties about the nuclear interaction between projectile and target are not expected to play a significant role. However, in order to correctly extract the information from cross sections, the accuracy of the description of the reaction mechanism must be ascertained.

Among halo nuclei, $^{11}$Be and $^{15}$C nuclei are of particular interest [2–4]. Because of the relative simplicity of their structure, the elaborate calculations required for a two-body breakup are not very affected by uncertainties about their wave functions. Indeed, their bound states can be fairly well described as a core to which a neutron is loosely bound. With a good approximation, the breakup can be seen as a transition from a two-particle bound state to the continuum, due to a varying Coulomb field. These nuclei are a good testing ground for approximate theories of Coulomb breakup.

In recent years a number of techniques have been developed for the calculation of Coulomb breakup: perturbation expansion [5–8], adiabatic approximation [9,10], coupled channels with a discretized continuum [11–14], and numerical resolution of the three-dimensional time-dependent Schrödinger equation [15–23]. Here we focus on the latter type of description where the projectile is assumed to follow a classical trajectory and its interaction evolves because of the varying Coulomb and nuclear fields of the target. These numerical resolutions, though much heavier, do not rely on assumptions about the magnitude of the different multipole fields or about the importance of higher-order effects. The main model assumptions are the validity of the semiclassical description of the projectile motion and the simplified description (shared by other models) of the internal structure of this projectile.

Recently, efficient mesh methods of numerical resolution of the time-dependent Schrödinger equation have been developed for accurately treating the time evolution of the projectile-nucleus wave function in this kind of reaction [15–17,19,20,23]. These analyses are performed with three spatial dimensions for the relative motion of the halo neutron with respect to the core. From a physical viewpoint, they are attractive owing to the simplicity of the treatment of time dependence. In principle, these methods are not restricted to purely Coulomb breakup and can take account of a nuclear component. However some of these methods have limitations. For example, the time-dependent Schrödinger equation is usually solved with a limited expansion in spherical harmonics followed by a discretization of the radial coordinate [16,17,19]. This approach requires an analytical treatment of the spherical harmonics. Matrix elements are calculated with a multipole expansion of the time-dependent potential between the halo nucleus and the target. They are often restricted to a few dominant multipoles [15–17,19]. The treatment of a nuclear interaction is more complicated than the treatment for the analytical Coulomb term. The purely numerical approach of Ref. [23] does not suffer from this difficulty but the use of a three-dimensional mesh in Cartesian coordinates prevents using $l$-dependent interactions and hence reproducing more than one bound state of a halo nucleus.

In this work, we apply a numerical technique of solution of the time-dependent Schrödinger equation on angular and radial meshes [24,25,20,21], which is free from the above-mentioned drawbacks. We express the formalism in the context of Lagrange meshes [26,27]. The wave function is ex-

 

panded over angular Lagrange functions associated with a two-dimensional angular mesh. The Lagrange functions vanish at all mesh points, except one. This basis is equivalent to a full set of spherical harmonics up to some orbital momentum complemented by selected harmonics beyond that value. It is used together with an associated Gauss quadrature, which eliminates the need for an analytical treatment. The simplicity of this method arises from the fact that the time-dependent potential matrix is diagonal when the Gauss approximation is used. The radial variable is discretized over a mesh with an increasing step obtained from a change of variables in a finite-difference technique.

The numerical technique is applied to the breakup of the $^{11}$Be and $^{15}$C halo nuclei at energies around 70 MeV/nucleon in order to make a comparison with experiments performed at RIKEN. At these energies, a fully numerical treatment is relevant because higher-order effects are not negligible and the interaction does not reduce to a single multipole. The role of the nuclear interaction with the target must also be evaluated. In Ref. [20], nuclear effects were simulated by a simple cutoff on impact parameters for the $^{11}$Be breakup. The validity and limitations of this approximation were not discussed.

In Sec. II, the time-dependent method is recalled. The computational algorithm for the time evolution is described in Sec. III. In Sec. IV, variants of radial meshes are compared and different tests are performed. In Sec. V, the internal potentials of the halo nuclei and optical potentials for a lead target are selected. The time evolution of the partial waves in the wave packet is depicted in Sec. VI. The obtained results are discussed in Sec. VII. The final section is devoted to concluding remarks.

## II. COULOMB BREAKUP BY TIME-DEPENDENT METHODS

We consider the breakup by the interaction with a target (with mass $m_T$ and charge $Z_T e$) of a two-body projectile made up of a pointlike core (with mass $m_c$ and charge $Z_c e$) and a pointlike fragment (with mass $m_f$ and charge $Z_f e$). In the projectile rest frame, the time-dependent Schrödinger equation can be written as

$$i\hbar \frac{\partial}{\partial t}\Psi(\mathbf{r},t)=H(t)\Psi(\mathbf{r},t)=[H_0(\mathbf{r})+V(\mathbf{r},t)]\Psi(\mathbf{r},t). \tag{1}$$

The Hamiltonian of the projectile reads

$$H_0(\mathbf{r})=-\frac{\hbar^2}{2\mu}\Delta+V_{cf}(\mathbf{r}), \tag{2}$$

where $\mu$ is the reduced mass of the core and fragment, $\mathbf{r}\equiv(\Omega,r)$ is the relative coordinate between them, and $V_{cf}$ is the internal interaction between the core and fragment of the projectile. This real potential, which may include Coulomb and spin-orbit terms, reads

$$V_{cf}(\mathbf{r})=V_0(r)+\mathbf{L}\cdot\mathbf{I}V_{LI}(r), \tag{3}$$

where $\mathbf{L}$ is the relative orbital momentum and $\mathbf{I}$ is the fragment spin. We assume that the spin $I_c$ of the core is zero and that the fragment spin $I$ is fixed. In other words, we neglect here the coupling with the core spin and core excitations.

The time-dependent potential is given by

$$V(\mathbf{r},t)=V_{cT}(r_{cT})+\frac{Z_c Z_T e^2}{r_{cT}}+V_{fT}(r_{fT})+\frac{Z_f Z_T e^2}{r_{fT}}-\frac{(Z_c+Z_f)Z_T e^2}{R}, \tag{4}$$

where $\mathbf{R}(t)$ is the time-dependent target position with respect to the projectile center of mass. The core-target and fragment-target coordinates read

$$\mathbf{r}_{cT}(t)=\mathbf{R}(t)+m_f\mathbf{r}/M, \tag{5}$$

$$\mathbf{r}_{fT}(t)=\mathbf{R}(t)-m_c\mathbf{r}/M, \tag{6}$$

respectively, where $M=m_c+m_f$ is the projectile mass. The complex optical potentials $V_{cT}$ and $V_{fT}$ describe the purely nuclear parts of the core- and fragment-target interactions. For simplicity, the point Coulomb interactions are displayed explicitly in Eq. (4). The core- and fragment-target Coulomb interactions could be replaced by more realistic form factors taking account of the finite sizes of the nuclei, without additional difficulty (see Sec. V B). In the projectile rest frame, the target follows a classical trajectory. This trajectory can be a straight line or a Coulomb trajectory. It could also be a trajectory taking nuclear effects into account [28], but we shall not make use of this case here. The initial velocity is denoted as $v$ and the impact parameter as $b$.

For partial wave $lj$, the projectile eigenstates (bound and scattering states) are defined by

$$H_0\phi_{ljm}(E,\mathbf{r})=E\phi_{ljm}(E,\mathbf{r}). \tag{7}$$

The projectile angular momentum $j$ results from the coupling of the orbital momentum $l$ with the fragment spin $I$. Negative energy states are normed and describe either the physical bound states of the projectile or states forbidden by the Pauli principle. Positive energy states correspond to the core-fragment scattering. They are necessary to analyze the final state of the system. The radial part of a scattering wave function is normalized in such a way that

$$R_{lj}(E,r)\underset{r\to\infty}{\to} r^{-1}[\cos\delta_l(E)F_l(E,r)+\sin\delta_l(E)G_l(E,r)], \tag{8}$$

where $F_l$ and $G_l$ are the standard regular and irregular Coulomb functions [29] and $\delta_l$ is the phase shift.

As an initial condition at $t=-\infty$, the system is in its ground state $l_0 j_0 m_0$ with energy $E_0<0$,

$$\Psi^{(m_0)}(\mathbf{r},-\infty)=\phi_{l_0 j_0 m_0}(E_0,\mathbf{r}). \tag{9}$$

The time-dependent wave function $\Psi^{(m_0)}(\mathbf{r},t)$ must be calculated for the different $m_0$ values. It also depends on the

impact parameter $b$, which is understood. The breakup probability per energy unit is given by

$$\frac{dP}{dE}(E,b)=\frac{2\mu}{\pi\hbar^2 k}\frac{1}{2j_0+1}\times\sum_{m_0}\sum_{ljm}|\langle\phi_{ljm}(E,\mathbf{r})|\Psi^{(m_0)}(\mathbf{r},+\infty)\rangle|^2, \tag{10}$$

where $k$ is the wave number [20]. It includes full distortion of the scattering eigenstates of the projectile. The breakup cross section reads

$$\frac{d\sigma_{\rm bu}}{dE}(E)=2\pi\int_0^\infty\frac{dP}{dE}(E,b)bdb. \tag{11}$$

When the nuclear interactions are neglected in Eq. (4), the lower bound in Eq. (11) is replaced by a cutoff $b_{\rm min}$ simulating these nuclear effects. Some authors [16,20,22,23] extract the breakup component from $\Psi^{(m_0)}(\mathbf{r},+\infty)$ before calculating the matrix elements appearing in Eq. (10). With exact scattering states, this additional projection is not necessary [21].

An inelastic scattering cross section to an excited bound state $nlj$ can be calculated as

$$\sigma_{nlj}(E)=2\pi\int_0^\infty P_{nlj}(b)bdb, \tag{12}$$

where

$$P_{nlj}(b)=\frac{1}{2j_0+1}\sum_{m_0}\sum_{m}|\langle\phi_{nljm}(E_{nlj},\mathbf{r})|\Psi^{(m_0)}(\mathbf{r},+\infty)\rangle|^2. \tag{13}$$

For pure Coulomb breakup, the probabilities satisfy the closure relation

$$\sum_{nlj}P_{nlj}(b)+\int_0^\infty\frac{dP}{dE}(E,b)dE=1. \tag{14}$$

The summation in this relation includes the forbidden states of the core-fragment potential, if any. The right-hand side of Eq. (14) becomes $\langle\Psi^{(m_0)}(\mathbf{r},+\infty)|\Psi^{(m_0)}(\mathbf{r},+\infty)\rangle$ when complex nuclear potentials are included in the time-dependent potential [Eq. (4)].

## III. APPROXIMATE TREATMENT OF TIME EVOLUTION

### A. Expansion in angular Lagrange functions

In the traditional approach, the time-dependent wave function is solved with an expansion in spherical harmonics $Y_l^m(\Omega)$. Here we describe a purely numerical approach without such a partial wave expansion [24,25,20,21]. However, we present it with a new notation in the spirit of the Lagrange-mesh method [26,27].

Let us start with $N$ points in a two-dimensional mesh on the unit sphere $\Omega_j=(\theta_{j'},\varphi_{j''})$ [24]. To this mesh are associated $N$ Gauss-quadrature weights $\lambda_j$ and $N$ Lagrange functions $f_j(\Omega)$. By construction, these functions satisfy the Lagrange property

$$f_i(\Omega_j)=\lambda_i^{-1/2}\delta_{ij}. \tag{15}$$

On this mesh, the Gauss-quadrature approximation reads

$$\int g(\Omega)d\Omega\approx\sum_{k=1}^N\lambda_k g(\Omega_k). \tag{16}$$

Hence, because of Eq. (15), the Lagrange functions are orthonormal at the Gauss approximation

$$\int f_i^*(\Omega)f_j(\Omega)d\Omega\approx\sum_{k=1}^N\lambda_k f_i^*(\Omega_k)f_j(\Omega_k)=\delta_{ij}. \tag{17}$$

The main interest of this basis is that the potential matrix is also diagonal at the Gauss approximation in angular space,

$$\begin{aligned}\int f_i^*(\Omega)V(\Omega,r,t)f_j(\Omega)d\Omega&\\ \approx\sum_{k=1}^N\lambda_k f_i^*(\Omega_k)V(\Omega_k,r,t)f_j(\Omega_k)&\\ =V(\Omega_i,r,t)\delta_{ij}.&\end{aligned} \tag{18}$$

The approximate matrix elements only depend on potential values at the angular mesh points.

How can such functions be constructed? Technical details and the definition of the mesh points and weights are given in the Appendix. The Lagrange functions are related with spherical harmonics. Let us consider $N$ functions $Y_\nu(\Omega)$ orthonormal at the Gauss approximation,

$$\int Y_\nu^*(\Omega)Y_{\nu'}(\Omega)d\Omega\approx\sum_{k=1}^N\lambda_k Y_\nu^*(\Omega_k)Y_{\nu'}(\Omega_k)=\delta_{\nu\nu'}. \tag{19}$$

The functions $Y_\nu(\Omega)$ involve standard spherical harmonics $Y_l^m(\Omega)$ for the lower $l$ values and modified ones $\tilde{Y}_l^m$ in the rest of the basis (see the Appendix for details). The last equality in Eq. (19) implies that matrix $\mathbf{S}$ with elements

$$S_{i\nu}=\lambda_i^{1/2}Y_\nu(\Omega_i) \tag{20}$$

is unitary. Hence one also has

$$\sum_{\nu=1}^N\lambda_i^{1/2}Y_\nu^*(\Omega_i)\lambda_{i'}^{1/2}Y_\nu(\Omega_{i'})=\delta_{ii'}. \tag{21}$$

The angular Lagrange functions are then given by

$$f_i(\Omega)=\lambda_i^{1/2}\sum_{\nu=1}^N Y_\nu^*(\Omega_i)Y_\nu(\Omega) \tag{22}$$

since these expressions satisfy the Lagrange condition (15) because of property (21).

The time-dependent wave function is expanded as

$$\Psi(\mathbf{r},t)=r^{-1}\sum_{m_I=-I}^{I}\sum_{i=1}^{N}\lambda_i^{1/2}f_i(\Omega)\psi_i^{m_I}(r,t)|Im_I\rangle. \quad (23)$$

At angular mesh points, Eq. (15) provides the explicit expression of a partial wave

$$\psi_i^{m_I}(r,t)=r\langle Im_I|\Psi(\Omega_i,r,t)\rangle. \quad (24)$$

With the column matrix $\mathbf{\Psi}$ with elements

$$\Psi_i(r,t)=\lambda_i^{1/2}\psi_i^{m_I}(r,t), \quad (25)$$

the matrix mesh equations read

$$i\hbar\frac{\partial}{\partial t}\mathbf{\Psi}(r,t)=[\hat{H}_0(r)+\hat{V}(r,t)]\mathbf{\Psi}(r,t). \quad (26)$$

The projectile Hamiltonian matrix $\hat{H}_0$ is diagonal with respect to index $l$ of basis $Y_\nu(\Omega)$,

$$\hat{H}_{0\nu\nu'}^{m_Im_I'}(r)=\left\{-\frac{\hbar^2}{2\mu}\left[\frac{\partial^2}{\partial r^2}-\frac{l(l+1)}{r^2}\right]+V_0(r)\right\}\delta_{m_Im_I'}\delta_{\nu\nu'} +\langle lm\,Im_I|\mathbf{L}\cdot\mathbf{I}|lm'Im_I'\rangle V_{LI}(r)\delta_{m_I+m,m_I'+m'}\delta_{ll'}. \quad (27)$$

When a spin-orbit force is used, it is not diagonal with respect to the spin projection $m_I$. In Eq. (27), the angular matrix elements $\langle Y_\nu|\mathbf{L}^2|Y_{\nu'}\rangle$ are replaced by $l(l+1)\delta_{\nu\nu'}$. This is not exact for the higher $l$ values (see the Appendix). The accuracy of this approximation seems to be consistent with the accuracy of the angular Gauss quadrature employed hereafter for the time-dependent interaction. A similar approximation is performed in the spin-orbit term.

The time-dependent interaction matrix $\hat{V}$ is fully diagonal in the Lagrange basis $f_i(\Omega)|Im_I\rangle$ [Eq. (18)] at the Gauss approximation,

$$\hat{V}_{ii'}^{m_Im_I'}(r,t)\approx V(\Omega_i,r,t)\delta_{ii'}\delta_{m_Im_I'}. \quad (28)$$

Hence it is convenient to use both bases in the calculation [20]. Changing bases is performed with matrix **S** [Eq. (20)].

### B. Radial discretization

The radial coordinate is discretized over a quasiuniform mesh,

$$r_j=r_{N_r}g(jh)/g(1), \quad j=1,...,N_r \quad (29)$$

obtained by mapping a uniform mesh with constant step $h=1/N_r$ over $x\in[0,1]$ onto $r\in[0,r_{N_r}]$ with a monotonic function $g(x)$, such that $g(0)=0$. Examples are given in Sec. IV A. The differentiation operators over $x$ can be discretized with the $(2n+1)$-point finite-difference formulas. The first-order derivative reads

$$\left(\frac{df}{dx}\right)_j\approx h^{-1}\sum_{k=-n}^{n}c_k^{(1)}f[(j+k)h], \quad (30)$$

with $c_0^{(1)}=0$ and, for $k\neq 0$,

$$c_k^{(1)}=(-1)^{k-1}\frac{(n!)^2}{k(n-k)!(n+k)!}, \quad (31)$$

i.e., $c_{-k}^{(1)}=-c_k^{(1)}$. The second derivative is given by

$$\left(\frac{d^2f}{dx^2}\right)_j\approx h^{-2}\sum_{k=-n}^{n}c_k^{(2)}f[(j+k)h], \quad (32)$$

with, for $k\neq 0$,

$$c_k^{(2)}=2c_k^{(1)}/k, \quad (33)$$

i.e., $c_{-k}^{(2)}=c_k^{(2)}$, and

$$c_0^{(2)}=-2\sum_{k=1}^{n}c_k^{(2)}=-2\sum_{i=1}^{n}i^{-2}. \quad (34)$$

After switching to coordinate $r$, one obtains

$$\left(\frac{d^2\psi}{dr^2}\right)_{r_j}\approx\left[\frac{g(1)}{hr_{N_r}g'(jh)}\right]^2\sum_{k=-n}^{n}\left[c_k^{(2)}-h\frac{g''(jh)}{g'(jh)}c_k^{(1)}\right]\psi(r_{j+k}). \quad (35)$$

Because of the factors depending on $jh$ and of the asymmetry of the coefficients $c_k^{(1)}$, the corresponding matrix and hence the representation on the mesh of operator $H_0$ are asymmetric.

On this mesh, radial integrals are approximated as

$$\int_0^\infty F(r)dr\approx\frac{hr_{N_r}}{g(1)}\sum_{j=1}^{N_r}g'(jh)F(r_j). \quad (36)$$

This relation is used to calculate the scalar product of two radial functions.

### C. Approximations of the evolution operator

The time evolution is obtained by an iteration with time step $\Delta t$. Let us start from the first term of the Magnus expansion [30],

$$\Psi(t+\Delta t)=\exp\left[-i\int_t^{t+\Delta t}H(t')dt'+O(\Delta t^3)\right]\Psi(t) \quad (37)$$

($\hbar=1$). For each time step, the evolution operator can be split as

$$\Psi(t+\Delta t)=\exp\left[-i\int_t^{t+\Delta t}V(t')dt'\right]\times\exp(-i\Delta tH_0)\Psi(t)+O(\Delta t^2). \quad (38)$$

With a simple approximation for the integral, one obtains

$$\Psi(t+\Delta t)=\exp[-i\Delta t V(t)]\exp(-i\Delta t H_0)\Psi(t)+O(\Delta t^2). \tag{39}$$

A better accuracy can, however, be obtained with the symmetrized expression [31]

$$\Psi(t+\Delta t)=\exp\left[-\frac{1}{2}i\int_t^{t+\Delta t}V(t')dt'\right]\exp(-i\Delta t H_0)\times\exp\left[-\frac{1}{2}i\int_t^{t+\Delta t}V(t')dt'\right]\Psi(t)+O(\Delta t^3). \tag{40}$$

Then the integrals must be approximated to order $\Delta t^3$, which can be done in several ways, such as

$$\Psi(t+\Delta t)=\exp[-\tfrac{1}{2}i\Delta t V(t+\tfrac{1}{2}\Delta t)]\exp(-i\Delta t H_0)\times\exp[-\tfrac{1}{2}i\Delta t V(t+\tfrac{1}{2}\Delta t)]\Psi(t)+O(\Delta t^3). \tag{41}$$

For example, one can verify that the less symmetric expression

$$\Psi(t+\Delta t)=\exp[-\tfrac{1}{2}i\Delta t V(t+\Delta t)]\exp(-i\Delta t H_0)\times\exp[-\tfrac{1}{2}i\Delta t V(t)]\Psi(t)+O(\Delta t^3) \tag{42}$$

has a similar accuracy.

After iteration over time, the order of the error changes since the number of mesh points is proportional to $1/\Delta t$. In fact, after iteration, the actual error of approximation (39) is of the same order $O(\Delta t^2)$ as the error of approximation (42). Indeed, with Eqs. (42) as well as with (39), the resulting algorithm reads

$$\begin{aligned}\Psi(t_n)=&\ldots\exp[-i\Delta t V(t_{j+1})]\exp(-i\Delta t H_0)\\&\times\exp[-i\Delta t V(t_j)]\exp(-i\Delta t H_0)\\&\times\exp[-i\Delta t V(t_{j-1})]\exp(-i\Delta t H_0)\ldots\Psi(t_0)\\&+O(\Delta t^2)\end{aligned} \tag{43}$$

with $t_j=t_0+j\Delta t$. Using Eqs. (39) or (42) differs by negligible corrections at the end points only. Other variants of this algorithm can be obtained by iterating Eq. (41), for example, but we did not observe significant differences between them.

The exponential operators are approximated as

$$\exp(-i\Delta t A)\approx(1+\tfrac{1}{2}i\Delta t A)^{-1}(1-\tfrac{1}{2}i\Delta t A)+O(\Delta t^3). \tag{44}$$

This approximation preserves unitarity and is consistent with Eqs. (41) and (42). The basic principle of the method relies on separate treatments of $H_0$ and $V(t)$ using different representations. The time evolution proceeds as follows. In a first half step, the factor depending on $H_0$ is treated in the basis $Y_\nu$ where the matrix operator $\hat{H}_0(r)$ is diagonal with respect to index $l$ [Eq. (27)],

$$[1+\tfrac{1}{2}i\Delta t\hat{H}_0(r)]\mathbf{\Psi}(r,t+\tfrac{1}{2}\Delta t)=[1-\tfrac{1}{2}i\Delta t\hat{H}_0(r)]\mathbf{\Psi}(r,t). \tag{45}$$

After discretization of $r$, the matrix $\hat{H}_0$ is a band matrix. The system (45) can thus be solved quickly [24]. It must be noted that in spite of the asymmetry of matrix $\hat{H}_0$, the norm of the wave function is conserved. Moreover, in the basis $Y_\nu$, a possible angular momentum dependence of potential $V_{cf}$ is easily taken into account.

In a second half step, the factor depending on the potential is propagated in the basis $f_j$ where the matrix operator $\hat{V}(r,t)$ is diagonal [Eq. (28)],

$$[1+\tfrac{1}{2}i\Delta t\hat{V}(r,t)]\mathbf{\Psi}(r,t+\Delta t)=[1-\tfrac{1}{2}i\Delta t\hat{V}(r,t)]\mathbf{\Psi}(r,t+\tfrac{1}{2}\Delta t). \tag{46}$$

After discretization of $r$, the matrix $\hat{V}$ is diagonal. Resolution is thus very fast. The algorithm implies a change of basis at each half step, which is fast since it only concerns the angular part.

## IV. NUMERICAL ASPECTS

### A. Radial mesh

The function defining the quasiuniform mesh used in previous works [20,21] reads

$$g_1(x)=e^{ax}-1. \tag{47}$$

Since $ah\ll 1$, the step exponentially increases from about $r_{N_r}ah\exp(-a)$ to about $r_{N_r}ah$.

Here we make use of a slightly more complicated expression

$$g_2(x)=ax+\ln\frac{\cosh[a(x-x_0)]}{\cosh(ax_0)}. \tag{48}$$

Both functions are monotonic with monotonic derivatives and vanish at 0. The first one has the drawback that the gap between successive points always increases and becomes too large near $r_{N_r}$ for the optimal choice of parameter $a$. Function $g_2$ has been devised to progressively switch from a small step to a slowly varying larger step. The parameter $x_0$ controls the location of the region along which the transition occurs. For $ax_0>1$, the step is about $r_{N_r}h(1-x_0)^{-1}\times\exp(-2ax_0)$ for small $x$ and about $r_{N_r}h(1-x_0)^{-1}$ for large $x$.

In Fig. 1 the step $r_j-r_{j-1}$ between two successive points of the radial grid is represented as a function of $r_j$ for both

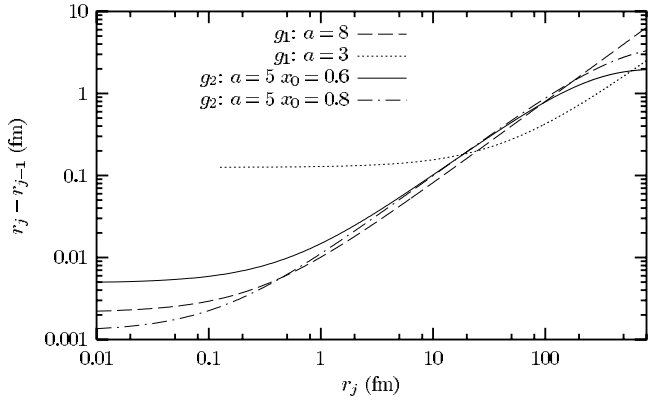


FIG. 1. Radial step as a function of $r_j$. Four different meshes are represented ($N_r=1000$, $r_{N_r}=800$ fm): $g_1$ distribution with $a=8$ (dashed line), $g_1$ distribution with $a=3$ (dotted line), $g_2$ distribution with $a=5$ and $x_0=0.6$ (full line), and $g_2$ distribution with $a=5$ and $x_0=0.8$ (dash-dotted line).

kinds of distributions $g_1$ and $g_2$. Distributions $g_1$ and $g_2$ exhibit the same behavior for small $r$: the initially small step increases, and the larger the parameter $a$ the faster the increase. But although the $g_1$ step continues to rise steadily for large $r$, the $g_2$ step progressively tends to a plateau. In order to illustrate the influence of the distribution on the evolution of the wave packet, Fig. 2 displays the modulus of the $s1/2 -1/2$ component of the final wave function obtained by the evolution algorithm. It corresponds to the projection of the wave packet on $|lIjm\rangle$ for $l=0$, $j=1/2$, and $m=-1/2$. The calculation is performed in the case of a $^{11}$Be projectile on a $^{208}$Pb target at an energy of 72 MeV/nucleon and at an impact parameter $b=25$ fm. It is performed for all the mesh-point distributions illustrated in Fig. 1.

The distribution shown as a dashed line in Fig. 1 corresponds to the mesh used in previous calculations [20,21], i.e., a $g_1$ distribution with $a=8$. The small step near $r=0$ allows a good description of the bound states of the two-body system but the steps near $r_{N_r}$ become too large ($>6$ fm), leading to a lack of precision in the description of the

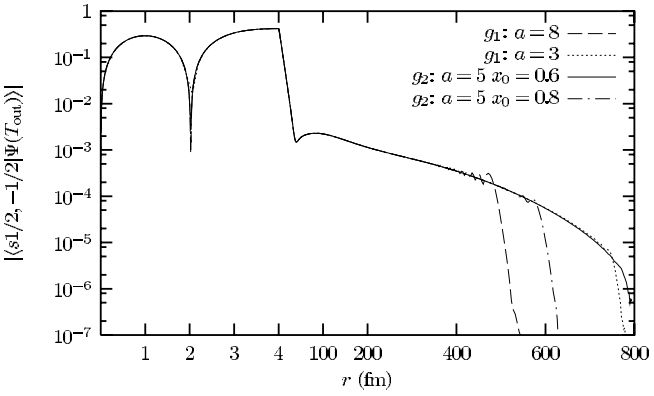


FIG. 2. Modulus of the $s1/2-1/2$ component of the $^{11}$Be wave function after evolution at $b=25$ fm and projectile energy 72 MeV/nucleon. Computations are done using the distributions depicted in Fig. 1. Note the change of abscissa scale at $r=4$ fm.

breakup component of the wave function. This explains the sudden fall of the corresponding wave function near $r=500$ fm in Fig. 2.

The same calculation is performed with a parameter $a=3$ so as to avoid too large a step at large distance (dotted line). The drop in the wave function modulus disappears and the wave function extends smoothly until the end of the radial grid but the radial step is larger than 0.1 fm near $r=0$, leading to a poor description of the bound states. This can be seen in Fig. 2 where the short-range behavior of the wave functions is represented at a larger scale than for the rest of the radial interval.

The results obtained with a $g_2$ distribution with $a=5$ and $x_0=0.6$ are depicted with full lines. This distribution allows a good description of the wave function at both small and large $r$. A calculation using $a=5$ and $x_0=0.8$ (dash-dotted lines) illustrates the influence of $x_0$ in the $g_2$ distribution. This distribution exhibits a smaller step near $r=0$ than the previous one but leads to a larger gap between points at large distance. The corresponding wave function is well described at short distances but exhibits a sudden drop near 600 fm due to too large a step near $r_{N_r}$.

The intervals of acceptable values of the parameters $a$ and $x_0$ seem to be relatively wide (i.e., $a\in[3,20]$ and $x_0\in[0.3,0.7]$). Inside these intervals, the choice of the parameters does not seem to influence much the evolution of the wave function. For the calculations below, we adopt $a=5$ and $x_0=0.6$.

The choice of the other parameters of the radial mesh is made as follows. Because of the time evolution process, the wave function which is initially a bound state of the halo nucleus develops a long-range breakup component (see Fig. 2 and Sec. VI). The maximal $r$ value $r_{N_r}$ has been chosen equal to 800 fm in order to avoid boundary effects. Most of the calculations presented below are done using $N_r=800$ in order to keep enough accuracy for the values of the cross section.

### B. Time interval and angular mesh

In the present study, all calculations are done assuming a straight line trajectory of the projectile,

$$\mathbf{R}(t)=\mathbf{b}+\mathbf{v}t, \tag{49}$$

where $\mathbf{b}$ is the impact vector and $\mathbf{v}$ is the initial velocity. The time $t=0$ corresponds to the closest approach of the projectile and target. We choose this parametrization instead of a Coulomb trajectory because the difference between a straight line and a hyperbola is negligible at the energies considered here as shown in Ref. [20]. More complicated trajectories can be introduced by solving the Schrödinger equation together with the classical Hamiltonian equations describing the relative projectile-target motion [28], but the effect is negligible at the energies considered here.

Time evolution starts at initial time $T_{\rm in}$ and stops at final time $T_{\rm out}$ by iteration over $N_T$ time steps $\Delta t$ as explained in Sec. III C. The initial (final) time has to be sufficiently negative (positive) so as to allow the time-dependent potential

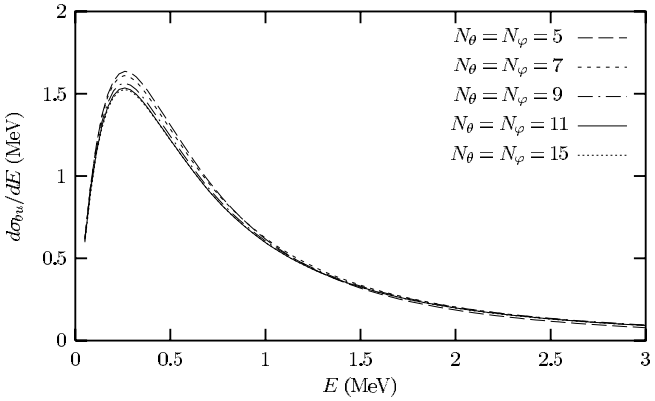


FIG. 3. Convergence with respect to the number $N_\theta = N_\varphi$ of angular mesh points in the $^{11}$Be case with the first optical potential of Table III at $v = 0.37c$.

$V(\mathbf{r},t)$ [see Eq. (4)] to be negligible at the beginning (end) of the evolution process. We select the same time interval as in Ref. [20]: $T_{\text{in}} = -20\hbar/\text{MeV}$ and $T_{\text{out}} = 20\hbar/\text{MeV}$. The time step $\Delta t$ is fixed equal to $0.02\hbar/\text{MeV}$.

In order to check the reversibility of the time evolution algorithm, we have performed a time-reversed calculation in which the initial wave function is the output function at $T_{\text{out}}$ after a normal evolution. In this test, the initial time is set equal to $T_{\text{out}}$ and the time step is chosen equal to $-\Delta t$ with the same number $N_T$ of time steps. The results of this calculation are astonishingly good: the wave function after the time-backward evolution is equal to the initial ground-state wave function of the time-forward evolution with an absolute error better than $10^{-13}$ at any mesh point.

At impact parameters where the breakup is purely Coulombic ($b > 30$ fm), the angular mesh is composed of 49 points: $N_\theta = 7$ for the $\theta$ variable and $N_\varphi = 7$ for the $\varphi$ variable. The corresponding basis includes all spherical harmonics up to $l = 3$ and some other up to $l = 9$ (see the Appendix). However the introduction of optical potentials representing the nuclear interactions with the target (Sec. V B) requires higher numbers of angular mesh points. The convergence with respect to $N_\theta = N_\varphi$ is studied in Fig. 3 with respect to a reference calculation with up to $N_\theta = N_\varphi = 15$ for some impact parameters. A fair accuracy is already obtained with $N_\theta = N_\varphi = 11$. This value is adopted in the rest of the calculations for $b < 30$ fm.

## V. TWO-BODY INTERACTIONS

### A. Core-fragment potential

Halo nuclei are treated here as two-body systems involving a pointlike core of spin 0 surrounded by a loosely bound neutron of spin 1/2. The potential $V_{cf}(\mathbf{r})$ [see Eq. (3)] is composed of a central term and a spin-orbit term coupling the neutron spin and the angular momentum of the neutron-core relative motion. Like in previous works [20,21], deep potentials are used. These potentials present unphysical bound states that simulate the occupied orbitals in the core. According to the Pauli principle, these bound states are forbidden to the fragment particle. As shown in Ref. [32], they play a negligible role in the breakup process and can therefore be ignored.

The central potential in Eq. (3) is chosen as

$$V_0(r) = -V_l f(r,R_0,a) \tag{50}$$

with a Woods-Saxon form factor

$$f(r,R_0,a) = \left[1 + \exp\left(\frac{r-R_0}{a}\right)\right]^{-1}. \tag{51}$$

The spin-orbit coupling term is expressed as

$$V_{LI}(r) = V_{LS}\frac{1}{r}\frac{d}{dr} f(r,R_0,a). \tag{52}$$

The parameters of the potentials are chosen so as to reproduce the bound states of the studied nuclei and, in the case of $^{15}$C, one of the resonances. Table I summarizes the experimental values on which the potentials are fitted.

In the case of $^{11}$Be we choose the same potential $V_{cf}$ as in Ref. [20] (adapted from Ref. [16]). In the case of $^{15}$C, we keep the same diffuseness ($a = 0.6$ fm) and radius ($R_0 = 1.2A^{1/3}$ fm) as for $^{11}$Be. The depths of the central and spin-orbit coupling terms are adapted so as to reproduce the energies of the two bound states and of the $3/2^+$ resonance. The values of the parameters used in the present work are listed in Table II. The bound-state and resonance energies obtained by the potentials described above are shown in Table I.

TABLE I. Experimental bound-state and resonance energies ($E_{\text{exp}}$), width ($\Gamma_{\text{exp}}$), and quantum numbers of the $^{11}$Be (Ref. [33]) and $^{15}$C (Ref. [34]) nuclei used to fit the parameters of the Woods-Saxon potential $V_{cf}$. The theoretical energies ($E_{\text{th}}$) and width ($\Gamma_{\text{th}}$) obtained with the parameters of Table II are also listed.

| $^{11}$Be | | | | $^{15}$C | | | | | |
|---|---|---|---|---|---|---|---|---|---|
| $J^\pi$ | $l$ | $E_{\text{exp}}$ (MeV) | $E_{\text{th}}$ (MeV) | $J^\pi$ | $l$ | $E_{\text{exp}}$ (MeV) | $\Gamma_{\text{exp}}$ (MeV) | $E_{\text{th}}$ (MeV) | $\Gamma_{\text{th}}$ (MeV) |
| $\frac{1}{2}^+$ | 0 | $-0.503$ | $-0.5013$ | $\frac{1}{2}^+$ | 0 | $-1.218$ | | $-1.2180$ | |
| $\frac{1}{2}^-$ | 1 | $-0.183$ | $-0.1844$ | $\frac{5}{2}^+$ | 2 | $-0.478$ | | $-0.4783$ | |
| | | | | $\frac{3}{2}^+$ | 2 | $3.56 \pm 0.1$ | $1.7 \pm 0.4$ | 3.25 | $\sim 1.7$ |

TABLE II. Parameters of the $n$-$^{10}$Be and $n$-$^{14}$C potentials.

| Nucleus | $V_{l=0}$ (MeV) | $V_{l>0}$ (MeV) | $V^{LS}$ (MeV fm$^2$) | $a$ (fm) | $R_0$ (fm) |
|---|---|---|---|---|---|
| $^{11}$Be | 59.5 | 40.5 | 32.8 | 0.6 | 2.669 |
| $^{15}$C | 52.814 | 51.3 | 20.77 | 0.6 | 2.959 |

### B. Projectile-target potentials

In previous works [20,21], the interaction between projectile and target is treated as purely Coulombic. The nuclear part of the interaction is simulated by an impact parameter cutoff. In the present work, calculations are performed with an optical potential modeling the projectile-target nuclear interaction.

The selected optical potentials between the projectile fragments and the target contain real and imaginary parts with Woods-Saxon form factors,

$$V_{xT}(r) = -Vf(r,R_R,a_R) - iWf(r,R_I,a_I), \qquad (53)$$

where $x$ stands for either $c$ (core) or $f$ (fragment). Point-sphere interactions replace the point Coulomb interactions in Eq. (4).

As in Ref. [22], the core-target potential $V_{cT}$ [see Eq. (4)] is scaled from the parametrization in Table 2 of Bonin *et al.* [35]. In order to evaluate the influence of the optical potential on the evolution of the wave function, we perform two calculations using both $^{10}$Be-$^{208}$Pb potentials listed in Table III.

The fragment-target optical potential $V_{fT}$ is taken from Becchetti, Jr. and Greenlees [36]. For a $^{208}$Pb target, the selected parameter values are given in Table III. Owing to the energy dependence of this potential, two neutron-target parameter sets are selected in order to allow a comparison with RIKEN experiments [2,4].

## VI. TIME EVOLUTION OF THE PROJECTILE-FRAGMENT WAVE PACKET

In order to illustrate the time evolution of the wave function, we present the final result of a breakup calculation for a $^{15}$C projectile on a $^{208}$Pb target at an impact parameter equal to 30 fm and a projectile velocity $v=0.36c$, corresponding to an energy of 68 MeV/nucleon. Figure 4 displays the results of that calculation for an initial function $\Psi(\mathbf{r},T_{\rm in})$ corresponding to the ground state $\phi_{s1/2-1/2}(E_0,\mathbf{r})$ (i.e., with $m_0=-1/2$). The time-dependent wave function is projected onto two different spin-angular states. The first one corresponds to the initial bound state ($s1/2-1/2$) and the second one to the most important contribution to the breakup component ($p3/2-3/2$). The wave function is depicted at times $t$ from $T_{\rm in}=-20\hbar/$MeV to $T_{\rm out}=20\hbar/$MeV at intervals of $5\hbar/$MeV. A similar figure for a $^{11}$Be projectile can be found in Ref. [37].

TABLE III. Parameters of the core-target (Ref. [35]) and neutron-target (Ref. [36]) optical potentials.

| $c$ or $f$ | $V$ (MeV) | $W$ (MeV) | $R_R$ (fm) | $R_I$ (fm) | $a_R$ (fm) | $a_I$ (fm) |
|---|---|---|---|---|---|---|
| $^{10}$Be (1) | 70.0 | 58.9 | 7.43 | 7.19 | 1.04 | 1.00 |
| $^{10}$Be (2) | 53.6 | 49.4 | 7.89 | 7.69 | 0.954 | 0.887 |
| $^{14}$C | 70.0 | 58.9 | 7.67 | 7.42 | 1.04 | 1.00 |
| $n$ (72 MeV) | 28.18 | 14.28 | 6.93 | 7.47 | 0.75 | 0.58 |
| $n$ (68 MeV) | 29.46 | 13.4 | 6.93 | 7.47 | 0.75 | 0.58 |

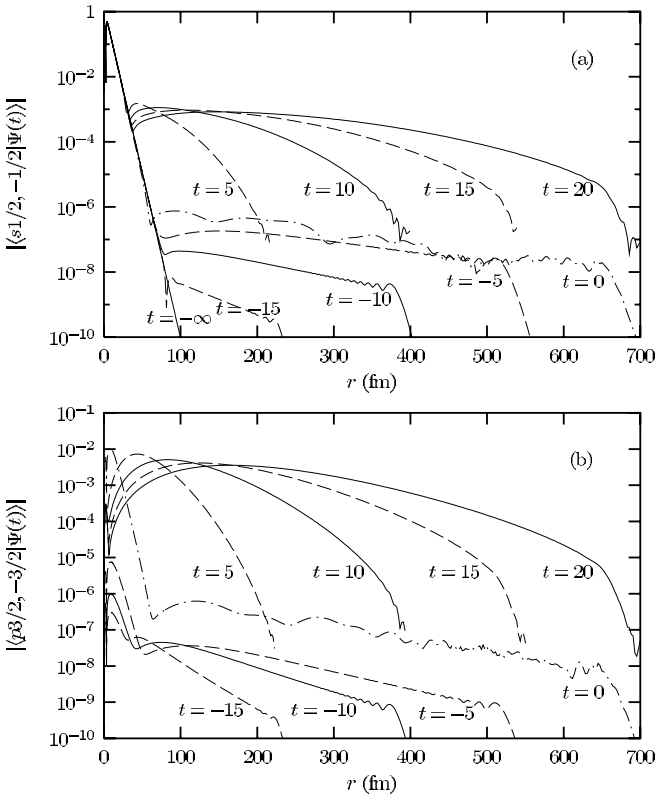


FIG. 4. Time evolution of the moduli of the (a) $s1/2-1/2$ and (b) $p3/2-3/2$ partial waves of the $^{15}$C breakup obtained with an initial $1s1/2-1/2$ bound state for $v=0.36c$ and $b=30$ fm.

At time $T_{\rm in}$, the halo nucleus is in its ground state with only a $s1/2-1/2$ component, which exhibits a characteristic exponential decrease. At later negative times, causality restricts modifications of the wave function induced by the projectile-target interaction to large $r$ values. Indeed, for $s1/2-1/2$, only the distant tail of the wave packet is affected. The $p3/2-3/2$ wave remains negligible at negative times. Near $t=0$, the partial wave functions start to change more deeply: some parts increase by several orders of magnitude. The modifications mainly correspond to the breakup component. The $p3/2-3/2$ wave becomes dominant at large distances. After the time of closest approach, the breakup component develops rather quickly towards large $r$ in both partial waves. It continues to spread as the wave packet evolves. In spite of this ongoing spreading, the low-energy breakup cross sections reach convergence near $T_{\rm out}$.

## VII. COULOMB BREAKUP CROSS SECTIONS

### A. Influence of nuclear interactions with the target

In the present section, we analyze the influence on the breakup probability (10) of the choice of the optical potential modeling the nuclear interaction between projectile and tar-

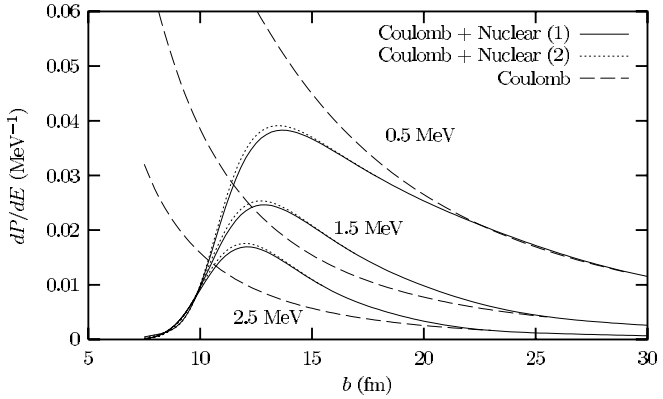


FIG. 5. Breakup probability per MeV of $^{11}$Be on a $^{208}$Pb target as a function of the impact parameter $b$ (in fm) for $E=0.5$, 1.5, and 2.5 MeV. Calculations are without optical potential between projectile and target (dashed lines), with the first (full lines) and second (dotted lines) $^{10}$Be-$^{208}$Pb potential of Table III, together with the neutron-target optical potential at 72 MeV.

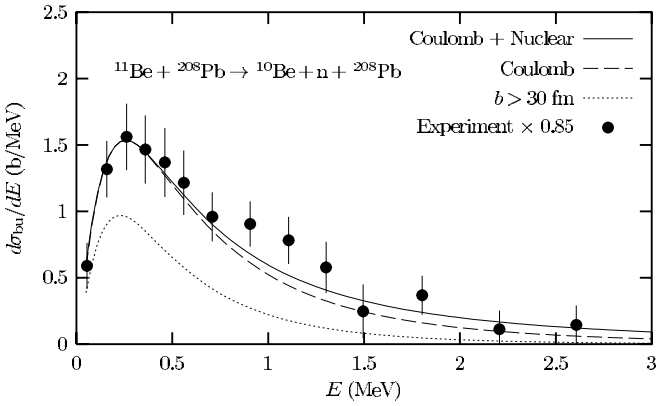


FIG. 6. Breakup cross sections (in $b$/MeV) as a function of the relative energy between the fragments of $^{11}$Be on $^{208}$Pb at 68 MeV/nucleon calculated with the $^{10}$Be-$^{208}$Pb and $n$-$^{208}$Pb optical potentials of Table III (full line) and with a cutoff at $b_{\min}=13$ fm (dashed line). Experimental results are from Ref. [2], but scaled by a factor 0.85 [38]. The dotted line corresponds to the cross section obtained for $b>30$ fm.

get. We also compare the effect of this interaction with the simpler model in which a minimum impact parameter $b_{\min}$ cuts off a purely Coulombic calculation in Eq. (11).

Introducing nuclear potentials is very simple in the present approach since it only requires values of these potentials at mesh points. Figure 5 shows the breakup probability of $^{11}$Be as a function of $b$ for three relative energies (0.5, 1.5, and 2.5 MeV). The calculation is done with an initial velocity $v=0.37c$ corresponding to a projectile energy of 72 MeV/nucleon. The evolution is computed in three different cases: (i) with the first $^{10}$Be-$^{208}$Pb optical potential and the neutron-$^{208}$Pb potential at 72 MeV of Table III (full lines), (ii) with the second $^{10}$Be-$^{208}$Pb optical potential and the same neutron-target interaction (dotted lines), and (iii) without optical potential between projectile and target (dashed lines).

The breakup probability obtained without optical potential monotonically decreases as a function of $b$. It diverges when $b$ tends to 0 as a consequence of the purely Coulombic nature of the interaction between projectile and target [see Eq. (4)]. In the calculations with an optical potential added to the projectile-target Coulomb interaction, the breakup probability is negligible near $b=0$ because of strong absorption. When approaching the range of absorption in the nuclear optical potential, the probability increases and reaches a maximum located around 11–14 fm. Beyond that maximum, at lower energies, the breakup probability remains smaller than that calculated without any optical potential. At energies larger than 0.5 MeV, the nuclear interaction with the target leads to a significant increase of the breakup probability. From $b=20-25$ fm, all results exhibit the same behavior as that without projectile-target nuclear interaction. The breakup probabilities obtained with both optical potentials are very close to each other.

The comparison of the breakup probabilities calculated with and without nuclear optical potential suggests that the cutoff impact parameter $b_{\min}$ should depend on energy in order to simulate nuclear effects. When we fit $b_{\min}$ to obtain the same breakup cross section in a pure Coulomb breakup approximation as in a calculation involving an optical potential, the $b_{\min}$ values calculated at the energies of Fig. 5 are 12.5 fm at 0.5 MeV, 9.1 fm at 1.5 MeV, and 6.9 fm at 2.5 MeV. Therefore the choice of an adequate impact parameter lower bound $b_{\min}$ in a cutoff approximation is not straightforward. Because of the simplicity of the present treatment, the modeling of the projectile-target nuclear interaction is better taken into account with an optical potential.

### B. Breakup of $^{11}$Be

The breakup cross section is calculated for a $^{11}$Be projectile on a $^{208}$Pb target. With the aim of comparing our theoretical results with the experimental ones of Nakamura *et al.* [2], the calculation is done at a velocity $v=0.37c$ with the numerical-parameter set given in Sec. IV. The cross sections obtained after time evolution are depicted in Fig. 6 for the different ways of simulating the nuclear interaction between projectile and target detailed above.

The cross sections obtained using both core-target optical potentials are indistinguishable. The Coulomb breakup cross section obtained with an impact parameter cutoff at $b=13$ fm (dashed line) is close to the cross section obtained with the optical potentials (full line) in the peak near 0.3 MeV. But, as stressed earlier, the difference between both calculations is energy dependent: the cross section including nuclear effects is systematically more important at high energy for this choice of cutoff. A similar result has been obtained in Ref. [22]. The data of Ref. [2] are scaled by a factor 0.85 according to a reanalysis of the experiment [38]. The comparison with our results shows good agreement between theory and experiment except around 1 MeV. The simplified description of $^{11}$Be here is essentially valid with a spectroscopic factor for the $n$-$^{10}$Be configuration in the $^{11}$Be ground state that is very close to unity.

The strong dominance of the $s$ wave agrees with several analyses of experimental results. However, the value of the spectroscopic factor and the importance of core excitation are still controversial. A measurement of the $^{11}$Be magnetic

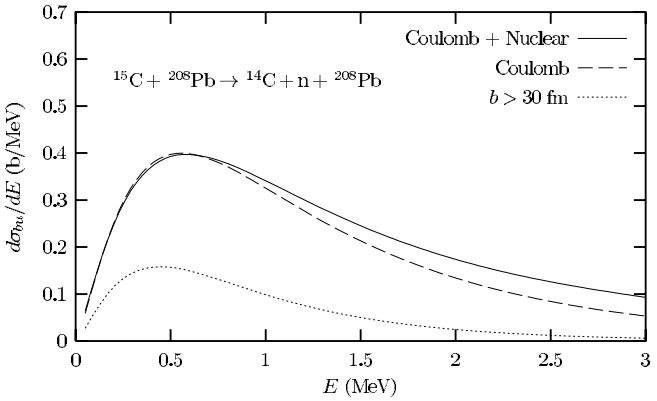


FIG. 7. Breakup cross sections (in $b$/MeV) as a function of the relative energy between the fragments of $^{15}$C on $^{208}$Pb at 68 MeV/nucleon calculated with the $^{14}$C-$^{208}$Pb and $n$-$^{208}$Pb optical potentials of Table III (full line) and with a cutoff at $b_{\min}=12.5$ fm (dashed line). The dotted line corresponds to the cross section obtained for $b>30$ fm.

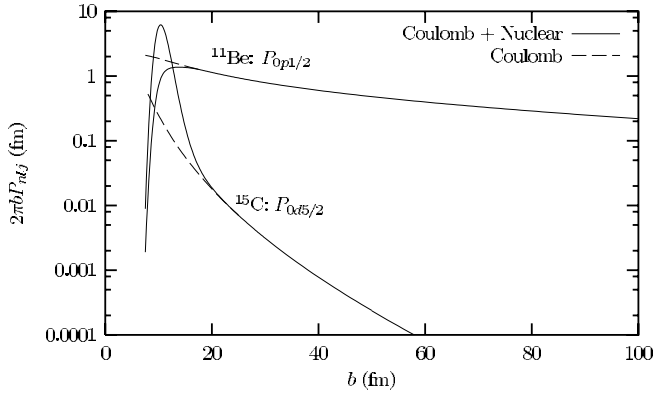


FIG. 8. Inelastic excitation cross sections on $^{208}$Pb to the $1/2^-$ state of $^{11}$Be at 72 MeV/nucleon and to the $5/2^+$ state of $^{15}$C at 68 MeV/nucleon calculated with optical potentials of Table III (full lines) and with pure Coulomb excitation (dashed lines).

moment is consistent with an almost pure $s$ state [39]. The $^{11}$Be$(p,d)^{10}$Be neutron-transfer reaction provides cross sections compatible with models involving 16% of $[2^+\otimes 0d]$ core excitation [40]. A study of neutron knockout from $^{11}$Be on $^{9}$Be is consistent with about 20% of core excitation [41]. However a reanalysis of these data leads to possibly smaller components [42]. Evaluating the importance of the spectroscopic factor from Coulomb breakup is difficult because of the sensitivity of its value to the adopted normalization of the experimental data. Precise statements have to wait for the publication of the new RIKEN data [4].

In order to determine the spectroscopic factor, it is also important to eliminate the effects of the nuclear interaction with the target. To this end, cross sections restricted to $b>30$ fm are shown as dotted lines in Fig. 6. They correspond to pure Coulomb breakup and can be measured [4].

### C. Breakup of $^{15}$C

The same kind of study is performed for the $^{15}$C halo nucleus using the numerical-parameter set of Sec. IV. The breakup cross sections with a $^{208}$Pb target are calculated at an energy of 68 MeV/nucleon ($v=0.36c$). That energy is chosen with the aim of providing results that can be compared in the near future with still unpublished RIKEN data [4].

In Fig. 7, two sets of results are shown. The first one includes all impact parameters and the second one corresponds to an integration of the breakup probability over impact parameters $b$ larger than 30 fm. The calculation of the breakup cross sections of $^{15}$C is done using the $^{14}$C-$^{208}$Pb optical potential and the $n$-$^{208}$Pb potential at 68 MeV listed in Table III (full line). These results are compared with the cross section obtained with a cutoff at $b_{\min}=12.5$ fm (dashed line). The pure Coulomb cross section calculated for $b>30$ fm is drawn as a dotted line. This quantity is now also accessible to experiment [4] and should allow determination of the spectroscopic factor of the $n$-$^{14}$C configuration in the $^{15}$C ground state.

As mentioned earlier, the difference between the cross sections obtained with an impact parameter cutoff and that calculated using an optical potential is energy dependent. Here also a rather large cutoff, 12.5 fm, reproduces the peak region near 0.6 MeV but underestimates the cross sections at higher energies. The calculation in Fig. 7 agrees fairly well with unpublished preliminary experimental data of Ref. [4]. They seem to indicate the need for a spectroscopic factor slightly smaller than unity.

### D. Comparison of the $^{11}$Be and $^{15}$C breakups

The $^{11}$Be and $^{15}$C nuclei are both weakly bound halo nuclei with only two bound states. These bound states have extended neutron orbitals. A difference between these nuclei is that the bound states have opposite parities in $^{11}$Be and positive parities in $^{15}$C. Hence Coulomb excitations behave quite differently. This effect is illustrated in Fig. 8 where inelastic transition probabilities (multiplied by $2\pi b$) are compared.

The Coulomb excitation probabilities to the $5/2^+$ state of $^{15}$C are smaller than that for the $1/2^-$ state of $^{11}$Be because the dominant transition corresponds to an $E2$ multipole while it is $E1$ for $^{11}$Be. They also decrease much faster with $b$ because of the larger excitation energy $\Delta E$. This decrease is indeed roughly proportional to $\exp(-2b\Delta E/\hbar v)$ [21]. Another difference concerns the nuclear effects. For $^{11}$Be, the probabilities obtained with optical potentials are smaller than those with a pure Coulomb interaction at all impact parameters. For $^{15}$C, the small Coulomb probabilities are significantly enhanced by the nuclear force around 10 fm. A cutoff approximation cannot reproduce such an effect.

The total breakup cross sections obtained with optical potentials are 0.690b (first set of parameters) or 0.692b (second set) for $^{11}$Be at 72 MeV/nucleon. The pure Coulomb calculation with a cutoff at 11.5 fm provides the good approximation 0.689b. The cross section for $^{15}$C at 68 MeV/nucleon is 0.0164b.

The breakup cross sections of both halo nuclei are much closer to each other than the inelastic cross sections since they are both dominated by $E1$ transitions. The $^{11}$Be cross

section is nevertheless larger because of the smaller binding energy of this nucleus. For the same reason the maximum of the cross section is located at lower energies [2].

## VIII. CONCLUSION

A time-dependent Schrödinger equation describes the breakup of a projectile in the varying Coulomb and nuclear fields of a target in the semiclassical approximation. A numerical technique of resolution of this equation on angular and radial meshes has been applied to the breakups of $^{11}$Be and $^{15}$C halo nuclei on $^{208}$Pb at energies around 70 MeV/nucleon.

With respect to previous works [20,21] different improvements of the mesh technique have been introduced. The first one concerns the presentation of the method. We have reformulated it in a more general way where the accuracies of the different approximations can more clearly be identified. The second improvement is technical and concerns the radial discretization. We analyzed the advantages and drawbacks of two types of radial discretization. This analysis shows the importance of keeping a small step at small distances in the projectile while preventing this step from growing too much at large distances. A new radial distribution of mesh points seems to fulfill these conditions satisfactorily. A third improvement is the introduction of nuclear optical potentials between the fragments of the projectile and the target. This introduction is straightforward in the present approach and does not require any analytical calculation. For given numbers of mesh points, it does not increase the computing time significantly.

The time evolution of the wave packet is illustrated with the behavior of two important partial waves in the $^{15}$C case. A breakup component appears near the time of closest approach and continues to spread thereafter. Partial waves fed by $E1$ transitions become dominant. Extended radial meshes are necessary for a good description of the wave function at large distances after interaction with the target.

Breakup cross sections of $^{11}$Be and $^{15}$C on $^{208}$Pb are calculated with optical potentials simulating the nuclear part of the interaction between projectile and target [22]. This realistic approach is compared with the pure Coulomb approximation involving a cutoff on impact parameters [20,21]. With a cutoff near 13 fm, this approximation is very good for both nuclei at low relative energies near the cross section maximum. Above the energy of this maximum small impact parameters play a larger role and the effect of the nuclear interaction becomes more important. The cutoff approximation then underestimates the breakup cross sections except if the cutoff impact parameter is chosen as decreasing with energy.

Inelastic cross sections have different orders of magnitude for $^{11}$Be and $^{15}$C because of the contrasted parities of the excited states. Breakup cross sections are somewhat smaller for $^{15}$C than for $^{11}$Be because of a larger binding energy. The $^{11}$Be breakup cross sections are in fair agreement with RIKEN data [2] with the new absolute normalization [38]. The $n$-$^{10}$Be description of this nucleus seems to be sound with a spectroscopic factor close to unity. Data for the $^{15}$C breakup at these energies have been obtained but are not yet published [4]. Preliminary analyses seem to indicate a good agreement with our results provided that a spectroscopic factor slightly smaller than unity is used for the $n$-$^{14}$C configuration.

An accurate description of the breakup of halo nuclei can be obtained by solving numerically the time-dependent Schrödinger equation but with significant restrictions. The breakup only involves a single nucleon and the simplest model is used to describe the halo. This model has the merit of reproducing the energy of the bound states and the node structure of their wave functions, at the cost of an angular-momentum dependence of the potential. It does not allow treating core excitation. Our aim is to improve the model description of the one-neutron halo nuclei and even to study the breakup of two-neutron halo nuclei with the time-dependent approach. To reach these goals, significant improvements of the different parts of the algorithm (i.e., the angular, radial, and time discretizations) must be realized in order to reduce the computing times.

## ACKNOWLEDGMENTS

This text presents research results of the Belgian program P5/07 on interuniversity attraction poles initiated by the Belgian-state Federal Services for Scientific, Technical, and Cultural Affairs. P.C. acknowledges the support of the National Fund for Scientific Research (FNRS), Belgium.

## APPENDIX

In this appendix, we define the angular mesh points, weights, and Lagrange functions. The $N=N_\theta N_\varphi$ angular points (where $N_\varphi$ is an odd number) form a two-dimensional mesh defined as

$$\Omega_j=(\theta_{j'},\varphi_{j''}) \tag{A1}$$

with $j\equiv(j',j'')$. The $N_\theta$ angles $\theta_{j'}$ with $j'=-(N_\theta-1)/2$ to $(N_\theta-1)/2$ are zeros of a Legendre polynomial of order $N_\theta$,

$$P_{N_\theta}(\cos\theta_{j'})=0. \tag{A2}$$

They thus have the property

$$\cos\theta_{j'}=-\cos\theta_{-j'}. \tag{A3}$$

The $N_\varphi$ angles $\varphi_{j''}$ ($j''=1$ to $N_\varphi$) are uniformly spaced over $[0,\,2\pi]$ as

$$\varphi_{j''}=\pi(2j''-1)/N_\varphi. \tag{A4}$$

The $N$ Gauss weights appearing in the quadrature formula (16) are defined as

$$\lambda_j=\lambda_{j'}^{(\theta)}\lambda_{j''}^{(\varphi)} \tag{A5}$$

with the Gauss-Legendre weights [29]

$$\lambda_{j'}^{(\theta)}=2/[\sin\theta_{j'}P'_{N_\theta}(\cos\theta_{j'})]^2 \tag{A6}$$

and the Gauss-Fourier weights

$$\lambda_{j''}^{(\varphi)} = 2\pi/N_\varphi . \tag{A7}$$

The angular basis must satisfy property (19). The $N$ basis functions with index $\nu \equiv (l,m)$ read

$$Y_\nu(\Omega) = N_{lm} \tilde{P}_l^{|m|}(\theta) \exp(im\varphi), \tag{A8}$$

where $N_{lm}$ is a normalization factor and $\tilde{P}_l^m$ is a Legendre function or a function modified as explained below. One easily verifies with Eqs. (A4) and (A7) that the orthogonality property (19) is automatically satisfied by the factor depending on $\varphi$, i.e., relation

$$\sum_{j''=1}^{N_\varphi} \lambda_{j''}^{(\varphi)} \exp(-im\varphi_{j''}) \exp(im'\varphi_{j''}) = 2\pi\delta_{mm'} \tag{A9}$$

is exact [26]. For $l < N_\theta$, the $\tilde{P}_l^m$ are nothing but the standard associated Legendre functions $P_l^m$ [29]. The $Y_\nu(\Omega)$ do not differ from the traditional spherical harmonics $Y_l^m(\Omega)$. For $l \geqslant N_\theta$, the functions $\tilde{P}_l^m(\theta)$ must differ from associated Legendre functions in order to be orthonormal at the Gauss-quadrature approximation on the $\theta_{j'}$ mesh. All $\tilde{P}_l^m$ must satisfy the relations

$$\sum_{j'=-(N_\theta-1)/2}^{(N_\theta-1)/2} \lambda_{j'}^{(\theta)} \tilde{P}_l^{|m|}(\theta_{j'}) \tilde{P}_{l'}^{|m|}(\theta_{j'}) = \frac{1}{2\pi N_{lm}^2} \delta_{ll'} . \tag{A10}$$

This is automatically satisfied by associated Legendre functions with the same $|m|$ value for $l, l' < N_\theta$. Indeed the Gauss approximation is exact for polynomials in $\cos\theta_{j'}$ up to order $2N_\theta - 1$ and Eq. (A10) is then nothing but the exact orthogonality relation between Legendre functions. The polynomials $\tilde{P}_l^{|m|}$ have a parity $(-1)^l$ so that Eq. (A10) is also automatically satisfied when $l + l'$ is odd. The first modification must occur for $l = N_\theta$ where the normalization factor $N_{lm}$ of $Y_\nu$ differs from the standard normalization factor of the spherical harmonics. For $l = N_\theta + 1$, the polynomial $\tilde{P}_l^{|m|}$ is orthogonalized to $P_{l-2}^{|m|}$ with the Gram-Schmidt algorithm based on the scalar product (A10). For $l = N_\theta + 2$, the polynomial $\tilde{P}_l^{|m|}$ is orthogonalized to $P_{l-4}^{|m|}$ and $\tilde{P}_{l-2}^{|m|}$ with the same Gram-Schmidt algorithm, and so on.

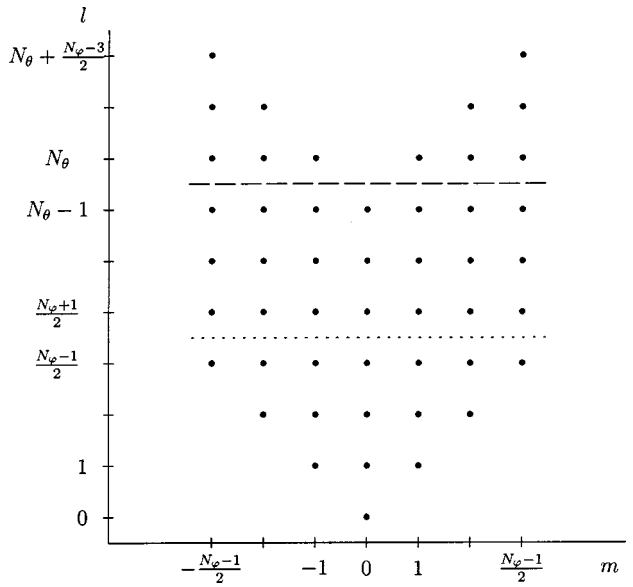


FIG. 9. Schematic representation of the $Y_\nu$ basis: each dot corresponds to a basis state. Up to $l = (N_\varphi - 1)/2$ (dotted line), all possible $Y_l^m$ are included. Below the dashed line, all basis functions are $Y_l^m$. Above this line, modified spherical harmonics are used.

The situation is depicted in Fig. 9. Up to $l = N_\theta - 1$, all $Y_\nu$ are standard spherical harmonics. For $l$ larger than $(N_\varphi - 1)/2$, $|m|$ values larger than $(N_\varphi - 1)/2$ are missing. Starting with $l = N_\theta$, modified Legendre functions are used: for $l$ equal to $N_\theta$, only the normalization of the spherical harmonics is modified; for $l$ larger than $N_\theta$, the functions $Y_\nu$ differ from spherical harmonics.


[1] I. Tanihata, J. Phys. G **22**, 157 (1996).

[2] T. Nakamura, S. Shimoura, T. Kobayashi, T. Teranishi, K. Abe, N. Aoi, Y. Doki, M. Fujimaki, N. Inabe, N. Iwasa, K. Katori, T. Kubo, H. Okuno, T. Suzuki, I. Tanihata, Y. Watanabe, A. Yoshida, and M. Ishihara, Phys. Lett. B **331**, 296 (1994).

[3] U. Datta Pramanik, T. Aumann, K. Boretzky, B. V. Carlson, D. Cortina, T. W. Elze, H. Emling, H. Geissel, A. Grünschloss, M. Hellström, S. Ilievski, J. V. Kratz, R. Kulessa, Y. Leifels, A. Leistenschneider, E. Lubkiewicz, G. Münzenberg, P. Reiter, H. Simon, K. Sümmerer, E. Wajda, and W. Walus, Phys. Lett. B **551**, 63 (2003).

[4] T. Nakamura, N. Fukuda, N. Aoi, H. Iwasaki, T. Kobayashi, T. Kubo, A. Mengoni, M. Notani, H. Otsu, H. Sakurai, S. Shimoura, T. Teranishi, Y. Watanabe, A. Yoshida, and M. Ishihara, in Proceedings of the International Symposium on the Physics of Unstable Nuclei, Halong Bay, Vietnam, 2002, edited by Dao T. Khoa *et al.*

[5] S. Typel and G. Baur, Phys. Rev. C **50**, 2104 (1994).

[6] H. Esbensen and G. F. Bertsch, Nucl. Phys. **A600**, 37 (1996).

[7] S. Typel, H. H. Wolter, and G. Baur, Nucl. Phys. **A613**, 147 (1997).

[8] S. Typel and G. Baur, Phys. Rev. C **64**, 024601 (2001).

[9] J. A. Tostevin, S. Rugmai, and R. C. Johnson, Phys. Rev. C **57**, 3225 (1998).

[10] P. Banerjee and R. Shyam, Phys. Rev. C **61**, 047301 (2000).

[11] M. Kamimura, M. Yahiro, Y. Iseri, H. Kameyama, Y. Sakuragi, and M. Kawai, Prog. Theor. Phys. Suppl. **89**, 1 (1986).

[12] N. Austern, Y. Iseri, M. Kamimura, M. Kawai, G. Rawitscher, and M. Yahiro, Phys. Rep. **154**, 125 (1987).

[13] J. A. Tostevin, F. M. Nunes, and I. J. Thompson, Phys. Rev. C **63**, 024617 (2001).

[14] J. Mortimer, I. J. Thompson, and J. A. Tostevin, Phys. Rev. C **65**, 064619 (2002).

[15] T. Kido, K. Yabana, and Y. Suzuki, Phys. Rev. C **50**, R1276 (1994).
[16] T. Kido, K. Yabana, and Y. Suzuki, Phys. Rev. C **53**, 2296 (1996).
[17] H. Esbensen, G. F. Bertsch, and C. A. Bertulani, Nucl. Phys. **A581**, 107 (1995).
[18] H. Esbensen and G. F. Bertsch, Phys. Rev. C **59**, 3240 (1999).
[19] S. Typel and H. H. Wolter, Z. Naturforsch., A: Phys. Sci. **54**, 63 (1999).
[20] V. S. Melezhik and D. Baye, Phys. Rev. C **59**, 3232 (1999).
[21] V. S. Melezhik and D. Baye, Phys. Rev. C **64**, 054612 (2001).
[22] S. Typel and R. Shyam, Phys. Rev. C **64**, 024605 (2001).
[23] M. Fallot, J. A. Scarpaci, D. Lacroix, P. Chomaz, and J. Margueron, Nucl. Phys. **A700**, 70 (2002).
[24] V. S. Melezhik, Phys. Lett. A **230**, 203 (1997).
[25] V. S. Melezhik, in *Atoms and Molecules in Strong External Fields*, edited by P. Schmelcher and W. Schweizer (Plenum, New York, 1998), p. 89.
[26] D. Baye and P.-H. Heenen, J. Phys. A **19**, 2041 (1986).
[27] D. Baye, M. Hesse, and M. Vincke, Phys. Rev. E **65**, 026701 (2002).
[28] V. S. Melezhik and P. Schmelcher, Phys. Rev. Lett. **84**, 1870 (2000).
[29] M. Abramowitz and I. A. Stegun, *Handbook of Mathematical Functions* (Dover, New York, 1970).
[30] R. M. Wilcox, J. Math. Phys. **8**, 962 (1967).
[31] M. Suzuki, J. Math. Phys. **26**, 601 (1985).
[32] P. Capel, D. Baye, and V. S. Melezhik, Phys. Lett. B **552**, 145 (2003).
[33] F. Ajzenberg-Selove, Nucl. Phys. **A506**, 1 (1990).
[34] F. Ajzenberg-Selove, Nucl. Phys. **A523**, 1 (1991).
[35] B. Bonin, N. Alamanos, B. Berthier, G. Bruge, H. Faraggi, J. C. Lucol, W. Mittig, L. Papineau, A. I. Yavin, J. Arvieux, L. Farvacque, M. Buenerd, and W. Bauhoff, Nucl. Phys. **A445**, 381 (1985).
[36] F. D. Becchetti, Jr. and G. W. Greenless, Phys. Rev. **182**, 1190 (1969).
[37] D. Baye, P. Capel, and V. S. Melezhik, in Proceedings of the International Symposium on the Physics of Unstable Nuclei, Halong Bay, Vietnam, 2002, edited by Dao T. Khoa *et al.*
[38] T. Nakamura (private communication).
[39] W. Geithner, S. Kappertz, M. Keim, P. Lievens, R. Neugart, L. Vermeeren, S. Wilbert, V. N. Fedoseyev, U. Köster, V. I. Mishin, V. Sebastian, and ISOLDE Collaboration, Phys. Rev. Lett. **83**, 3792 (1999).
[40] J. S. Winfield, S. Fortier, W. N. Catford, S. Pita, N. A. Orr, J. Van de Wiele, Y. Blumenfeld, R. Chapman, S. P. G. Chappell, N. M. Clarke, N. Curtis, M. Freer, S. Galès, H. Langevin-Joliot, H. Laurent, I. Lhenry, J. M. Maison, P. Roussel-Chomaz, M. Shawcross, K. Spohr, T. Suomijrvi, and A. de Vismes, Nucl. Phys. **A683**, 48 (2001).
[41] T. Aumann, A. Navin, D. P. Balamuth, D. Bazin, B. Blank, B. A. Brown, J. E. Bush, J. A. Caggiano, B. Davids, T. Glasmacher, V. Guimarães, P. G. Hansen, R. W. Ibbotson, D. Karnes, J. J. Kolata, V. Maddalena, B. Pritychenko, H. Scheit, B. M. Sherrill, and J. A. Tostevin, Phys. Rev. Lett. **84**, 35 (2000).
[42] J. A. Tostevin, D. Bazin, B. A. Brown, T. Glasmacher, P. G. Hansen, V. Maddalena, A. Navin, and B. M. Sherrill, Phys. Rev. C **66**, 024607 (2002).